nature communications

Article

https://doi.org/10.1038/s41467-024-53461-5

Light-modulated van der Waals force microscopy

Received: 22 October 2023

Accepted: 14 October 2024

Published online: 22 October 2024

Check for updates

Yu-Xiao Han, Benfeng Bai ✉, Jian-Yu Zhang, Jia-Tai Huang, Peng-Yi Feng & Hong-Bo Sun ✉

Atomic force microscope generally works by manipulating the absolute magnitude of the van der Waals force between tip and specimen. This force is, however, less sensitive to atom species than to tip-sample separations, making compositional identification difficult, even under multi-modal strategies or other atomic force microscopy variations. Here, we report the phenomenon of a light-modulated tip-sample van der Waals force whose magnitude is found to be material specific, which can be employed to discriminate heterogeneous compositions of materials. We thus establish a near-field microscopic method, named light-modulated van der Waals force microscopy. Experiments discriminating heterogeneous crystalline phases or compositions in typical materials demonstrate a high compositional resolving capability, represented by a 20 dB signal-to-noise ratio on a $MoTe_2$ film under the excitation of a 633 nm laser of 1.2 mW, alongside a sub-10 nm lateral spatial resolution, smaller than the tip size of 20 nm. The simplicity of the light modulation mechanism, minute excitation light power, broadband excitation wavelength, and diversity of the applicable materials imply broad applications of this method on material characterization, particularly on two-dimensional materials that are promising candidates for next-generation chips.

Since the early speculation by Binnig, Quate and Gerber in 1985, atomic force microscope (AFM)[1] has been established as a unique characterization tool with spatial resolution more than 1000 times better than the optical diffraction limit[2–4]. It utilizes mainly van der Waals (vdW) force[5], F_v, between the sharp tip apex of a cantilever and the specimen surface for force measurement and morphology mapping. Although vdW force is the weakest among the long-range forces, it is sensitive to distance between atoms, r, by law of $F_v \sim r^{-7}$. This leads to, on the one hand, a vertical resolution high enough to recognize single-atom steps[6,7], and on the other hand, the difficulty in compositional identification at ambient temperature and atmosphere, such as the heterogeneous phases in mono- or few-layer two-dimensional (2D) semiconductors[8,9], due to the morphological perturbation.

For the purpose of composition recognition, alternative strategies have been developed[10,11]. For example, AFM-based infrared spectroscopy (AFM-IR)[12] resorts to molecular resonant absorption in infrared to locally swell sample surface, and scanning near-field optical microscope (SNOM)[13,14] monitors fluorescence or Raman scattering from the sample. Both reach the end to some extent but lose the simplicity or versatility of AFM, for the price of needing multiple wavelengths to match particular infrared absorption peaks of different materials (AFM-IR) or requiring spectrometers for wavelength separation (SNOM). Multi-modal AFM goes further along this line. Rodríguez and García[15] found that by simultaneously exciting fundamental and high-order vibration modes of a cantilever, material compositions were distinguishable from the phase imaging of the latter. Despite the success of bi-modal AFM in, for example, KBr (001)[16], flexible crystals [$Cu(acac)_2$][17], human teeth[18], metal organic framework[19,20], and single IgM antibody protein[21] imaging, it is suffering from the sensitive dependence on the intrinsic property discrepancy of compositional materials for sufficient phase contrast and is only applicable to limited types of materials.

State Key Laboratory of Precision Measurement Technology and Instruments, Department of Precision Instrument, Tsinghua University, 100084 Beijing, China. ✉e-mail: baibenfeng@tsinghua.edu.cn; hbsun@tsinghua.edu.cn

Here, we report a phenomenon, called the light-modulated vdW force (LvF), which leads to an effective solution to the challenge of compositional identification with AFM. The force is attributed to asymmetric force variation due to the −7th power dependence on tip-sample distance[22] when sample surface atoms approach nearer and depart further from the AFM tip with greater amplitude in thermal motion enhanced by the light-modulated optothermal effect. The net force increment is found sensitively dependent on materials, laying the physical foundation for the concept of light-modulated van der Waals force microscopy (LvFM). The effectiveness of LvFM lies in involving intermolecular bonding forces of materials[23] in addition to the tip-sample vdW force, and magnifying the difference of intrinsic material characteristics by light excitation. A high compositional resolving power and a sub-10 nm lateral spatial resolution can thus be achieved. A detailed comparison of LvFM with other near-field microscopic methods is discussed in Supporting Information, SI-1.

Results

Two types of atomic forces

Both vdW force and chemical bonding force are widely known atomic forces existing in materials to bind atoms or molecules into condensed phase[24]. The former, often appearing as an inter-molecular force, governs the stability of colloids and dominates energies of surfaces and interfaces[25]; while the latter, for the sake of brevity, bonding force, creates mechanical resist against compression, extension, bending and distortion of solid materials[26]. The vdW force is produced due to transient separations of positive and negative centers in neutrally charged atoms, molecules or particles, which pairwise induce dipoles spontaneously in a neighboring object, acting to and reacting on it[5]. The second-order-perturbation nature of the transient dipole pair interaction results in sharp, −6th power in potential and −7th power in force, dependence on separation. The bonding force, on the other hand, arises in nature from strong Coulombic interactions among positively charged atomic cores and redistributed negative valence electron clouds[27]. It presents either attractive or repulsive depending on whether a solid sample is pulled long or compressed. The repulsive bonding force also appears when a probe tip approaches a sample surface within the lattice constant proximity, with a -13^{th} power dependence on separation. The total inter-molecular forces are represented by[22],

$$f_{LJ} = 12\frac{\varepsilon}{r_0}\left(\frac{r_0^7}{r^7} - \frac{r_0^{13}}{r^{13}}\right), \quad (1)$$

where ε, r_0, and r are the bond energy of Lennard-Jones potential, the inter-atomic distance at potential equilibrium, and the practical inter-atomic distance, respectively. The first term at the right side of Eq. (1) is an attractive vdW force (F_v) and the second is a repulsive bonding force (F_B), which are schematically shown in Fig. 1a. The repulsive bonding force F_B affects the engagement factor (oscillation amplitude) of an

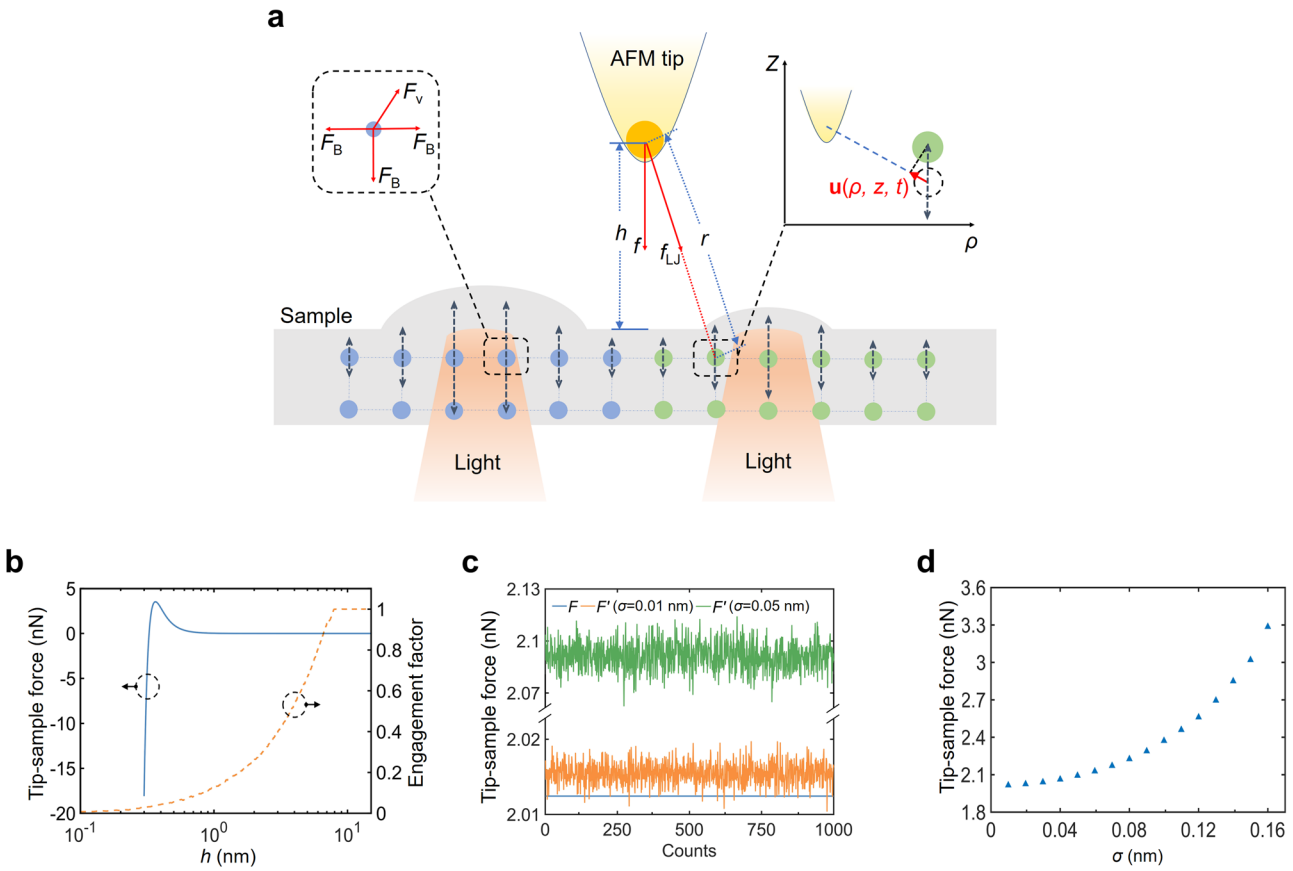

Fig. 1 | Physical origin of LvF. a Schematic of the vdW force (F_v) interactions between an AFM probe tip and a sample surface when their distance is small enough. The LvF is excited and enhanced by a modulated light due to the intensified molecular thermal motions of the sample, where the normal components of their motions are indicated by vertical arrows. The LvF strength is sensitively dependent on materials due to their different bonding forces (F_B). The blue and green disks indicate two types of material molecules under identical illumination. The insets show the local coordinates, position vector of a molecule, and forces. **b** Calculated total tip-sample force F versus tip-sample distance h (blue) and the practical engagement factor (tapping amplitude) of an AFM probe versus h (orange). In calculation, $\varepsilon = 1 \times 10^{-19}$ J, $r_0 = 0.3$ nm, and the tip radius $R = 10$ nm. **c** Monte Carlo simulations of the total LvF (F') when $\sigma = 0.01$ nm and $\sigma = 0.05$ nm. The curve of F without light excitation is provided for comparison. The tip-sample distance is fixed as 1 nm in simulation. **d** F' versus different intensities of molecular thermal motions described by σ. The value of F' at each σ is the average of 1000 times Monte Carlo simulations.

AFM cantilever in tapping mode[28] (Fig. 1b) when it approaches the sample surface, which is utilized as a measure in LvF detection. More discussions about the tip-sample interaction forces are given in Supporting Information, SI-2.

It is worth mentioning that the vdW force occurring between identical and alien atoms or molecules is generally less than the attractive bonding force by orders[27], and their huge difference in magnitude explains why they are seldom mutually adopted to characterize materials and their interactions. The dilemma of composition identification in AFM arises from the fact that only vdW interactions between the tip and specimen are employed, which reflects partial characters of matter to be detected. The bonding force, F_B, indiscriminately imposed on surface atoms by their neighborhood beneath, is playing an even more important role in materials performance and their response to external stimuli. If it is boosted and appropriately included in characterization, together with vdW force, a way may be paved towards effective compositional identification. Here, the mismatch has actually been overcome by light excitation on the bonding force, which affects the thermal motions of the molecules or atoms on sample surface. It is the bonding force change, instead of the force itself, that becomes comparable to the vdW force, and further contributes to the occurrence of LvF.

Light-modulated vdW force

The tip-sample vdW force can be modulated and enhanced when a laser is focused beneath the tip on a sample, as is manifested analytically and numerically below.

The vdW force F between an AFM tip and a sample requires integrating the dipole interactions over the entire volume of the tip (whose profile can be regarded as a hemisphere) and the infinite semispace of the sample surface,

$$F = \int n_1 dV_1 \left(\int n_2 dV_2 \cdot f_{LJ} \right) = \int n_1 dV_1 \cdot f \tag{2}$$

where n and V represent the dipole (atom) density and integral volume of the probe tip (subscript 1) or the sample (subscript 2), respectively; f and F are the force between a certain atom in the tip and the whole specimen and the entire tip-sample force, respectively. Numerical calculation of F can be performed with the procedure detailed in Supporting Information, SI-3. Figure 1b shows the numerically calculated total tip-sample force F versus the tip-sample distance h as well as the engagement factor (tapping amplitude) of a probe with respect to h, by taking $\varepsilon = 1 \times 10^{-19}$ J, $r_0 = 0.3$ nm, and tip radius $R = 10$ nm. The h sensitive feature of the tip–sample force and its impact on the engagement factor of the probe in the vdW force interaction zone are clearly observed.

When a light beam illuminates the sample surface, the thermal motions of the sample molecules are intensified due to the absorption of light, which are specific to materials, as schematically shown in Fig. 1a. To describe the irregular thermal motion of a molecule located at (ρ, z) and at moment t, we can define a random displacement vector $\mathbf{u}(\rho, z, t)$, as shown in the inset of Fig. 1a, whose direction is always along $\mathbf{r}$, i.e., toward the tip apex. The temperature rise caused by optothermal effect in a material, as a manifestation of the intensified thermal motions of molecules, can be theoretically analyzed as described in Supporting Information, SI-4. Then the force f is changed to

$$f' = \iiint_{\Omega} n_2 \mathbf{f}_{LJ}(r + u(\rho, z, t)) \cdot \mathbf{n} dV \triangleq \frac{\pi n_2 \varepsilon r_0^6}{12(h - \Delta h)^4}, \tag{3}$$

where $\mathbf{f}_{LJ}(r + u(\rho, z, t))$, $\mathbf{n}$, h, and Δh are the vector of Lennard-Jones force, the unit vector of sample surface normal, the tip-sample distance, and the variation of the tip-sample distance due to light excitation, respectively, and Ω is the entire sample volume. Detailed derivation of Eq. (3) is given in Supporting Information, SI-5. According to Eq. (3) and referring to Fig. 1a, one can find that when a sample molecule moves closer to the probe tip under light excitation, the vdW force f' increases, due to the decrease of the tip-molecule distance to $h - \Delta h$; on the contrary, when the molecule moves farther away from the tip in the other half of its oscillation cycle, f' decreases due to the increase of $h + \Delta h$. Having obtained f', we can substitute Eq. (3) into Eq. (2) and calculate the total tip-sample LvF, denoted as F', by numerical integration. Since f' has a high-order nonlinear dependence ($\propto h^{-4}$) on h, the integration of f' in one cycle of the molecule oscillation should lead to the increase of the overall time-averaged tip-molecule vdW force F', as numerically validated below.

We perform Monte Carlo simulations[29] using the theoretical model developed above. A variance σ of $u(\rho, z, t)$ is introduced to describe the extent of random motion of the molecule, which is correlated to the power of incident light. The random thermal motions of molecules are assumed to follow Cauchy distribution, whose mathematical expectation is 0, reflecting the fact that the thermal motions are always around the mass centers of the molecules. When σ is taken as 0.01 nm, 1000 molecular dynamic simulations are performed to obtain the magnitude of LvF, as shown by the orange curve in Fig. 1c, where $F' > F$ occurred 982 times and $F' < F$ occurred only 18 times. This confirms that light excitation does enhance the tip-sample force. Specifically, the time-averaged F' is 2.0155 nN, which has a 0.15% increment over $F = 2.0124$ nN. When σ is further increased to 0.05 nm, the obtained F' is increased by 3.94%, as shown by the green curve in Fig. 1c. Figure 1d demonstrates the calculated data of F' with respect to different values of σ, showing that F' increases exponentially with the increase of the excitation light power. All these analyses confirm that the tip-sample vdW force can be enhanced by the optothermal effect due to the absorption of excitation light, which is the origin of LvF and can be utilized to discriminate different materials by probing their distinct LvF responses.

Picking up of LvF signals

Since the weak LvF signal is obscured by other tip-sample forces and background noises, it is difficult to detect the LvF directly. To solve this problem, we propose to use a dual-modal cantilever (with fundamental and second-order resonance frequencies f_1 and f_2) working in tapping mode and employed a sideband demodulation technique to extract the LvF signal, along with the topography mapping.

Instrumentally, we establish a home-built system based on an AFM platform and equip it with an inverted optical microscope (Fig. 2a, b). The probe installed on a dual-modal cantilever is driven by a dither piezo at frequency f_1. A laser beam modulated at frequency f_m is focused onto the sample and illuminates it from the bottom. Coupling of forces between f_1, originating from the tapping, and f_m, from LvF results in beating frequencies of $f_2 = |f_m \pm f_1|$ (as shown in Fig. 2c). Since f_2 is the second-order resonance frequency of the cantilever, the maximum LvF signal can be demodulated at this frequency. To validate this scheme, we use a silicon probe with $f_1 = 235.7$ kHz, quality factor $Q_1 = 572$ and $f_2 = 1471.8$ kHz, $Q_2 = 756$. The setpoint of the proportional integral derivative controller, used to maintain a constant tip-sample distance during scan, is set as 60% of the free oscillation amplitude (~10 nm). This ensures that the probe enters the vdW force interaction zone in one oscillation cycle. The excitation laser is modulated at $f_m = f_2 - f_1 = 1236.1$ kHz. A monitoring laser beam is reflected from the back of the AFM cantilever and detected by a position sensitive detector (PSD). In this way, the cantilever oscillation is monitored and amplified by the optical lever as an electric signal, which is then split and demodulated by two lock-in amplifiers (Fig. 2a, b). One of them takes f_1 as the reference to measure the stationary surface morphology, while the other refers to f_2 provided by an electronic mixer mixing

https://doi.org/10.1038/s41467-024-53461-5

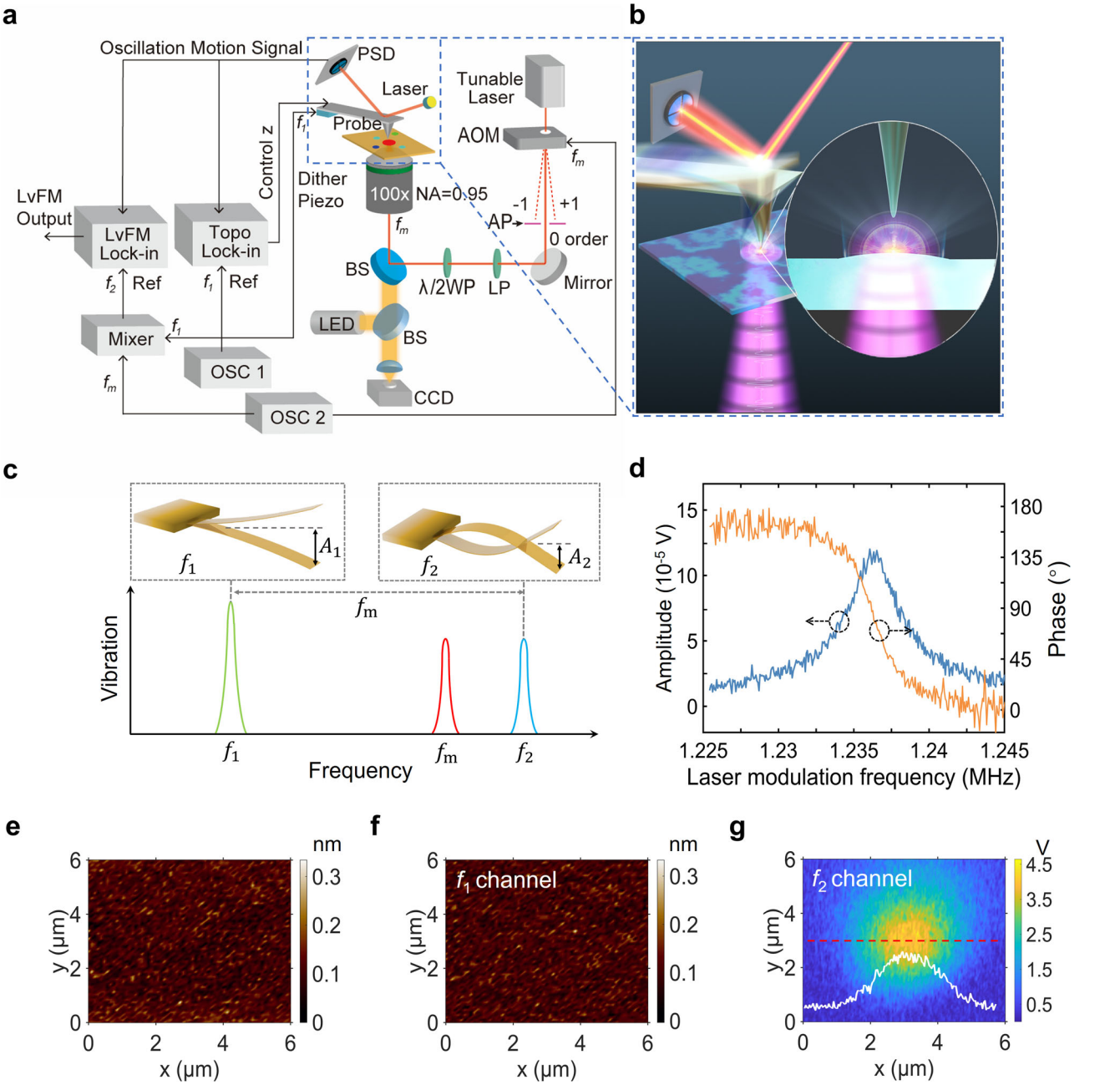

Fig. 2 | Instrumental realization of LvFM. a Schematic of the home-built LvFM setup. AOM: acousto-optic modulator; PSD: position sensitive detector; AP: aperture; WP: wave plate; LP: linear polarizer; BS: beam splitter; LED: light emitting diode; CCD: charge coupled device; NA: numerical aperture; Topo: Topography; OSC: oscillator; Ref: reference. f_1 is the tapping frequency of the probe. f_m is the modulation frequency of the illuminating laser. f_2 is the demodulation frequency of LvF. **b** Illustration of the LvFM working principle. The local LvF is detected by demodulating the AFM probe oscillation at f_2 that is amplified by an optical lever. **c** Illustration of an AFM cantilever with two mechanical resonance frequencies f_1 and f_2 and resonance amplitudes A_1 and A_2. The light modulation frequency f_m is chosen such that $f_2 = |f_m \pm f_1|$. **d** Measured LvF response of a borosilicate glass with a silicon probe, which shows the amplitude and phase curves of the LvF signal versus the laser modulation frequency f_m when the tapping frequency is fixed at f_1. **e** Topography image of a borosilicate glass sample measured by a commercial AFM. **f** Topography image and **g** LvF image of the borosilicate glass sample measured by the LvFM setup with an excitation 633 nm laser of 1.2 mW. The white curve is the profile of LvF signal amplitude along the red dashed line.

f_m and f_1 to detect the LvF signal. More details about the dual-modal cantilever are given in Supporting Information, SI-6. Since the amplitude and phase of the LvF signal are demodulated at f_2 while the tapping frequency is fixed at f_1, we can scan the laser modulation frequency f_m to check the best demodulation frequency, as shown in Fig. 2d. Clearly, the signal maximum appears around 1236 kHz, which is exactly the value of $f_m = f_2 - f_1$, exhibiting the effectiveness of the dual-channel signal picking up. More details about the sideband demodulation are provided in Supporting Information, SI-7.

Having established the LvFM system, we can use it to detect LvF responses of samples. As the first experiment, we prepared a flat borosilicate glass substrate as a sample, whose surface roughness was at sub-nanometer level, as measured by a commercial AFM (Fig. 2e). When a 633 nm laser of 1.2 mW illuminated the glass substrate surface,

https://doi.org/10.1038/s41467-024-53461-5

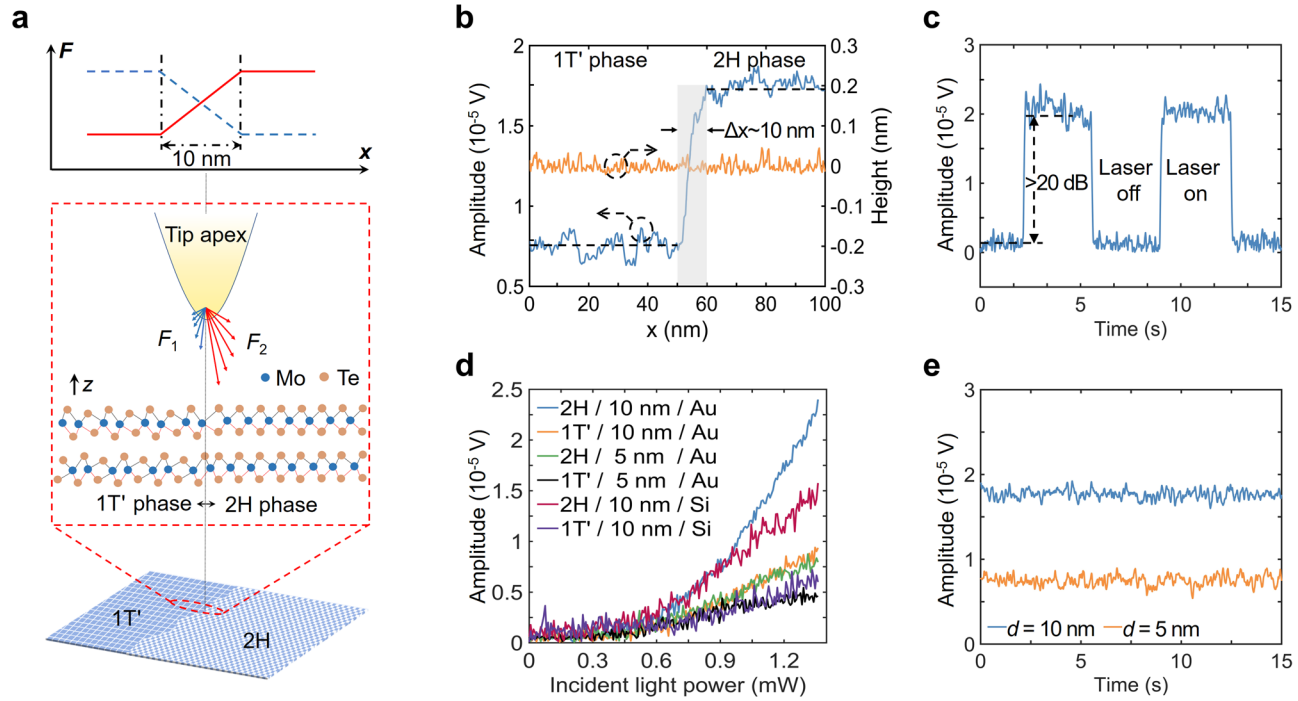

Fig. 3 | Spatial resolution and compositional resolving capability of LvFM. **a** Schematic illustration of the two crystalline phases 2H and 1T′ in a $MoTe_2$ film, where F_1 and F_2 represent the LvFs exerted on the tip from the 1T′ and 2H phases when the tip crosses their boundary. The force may increase (solid red line for F_2, the top inset) or decrease (dashed blue line for F_1) depending on materials. **b** Measured LvF profile (blue line) and topography (orange line) when the probe scans across a boundary of the 2H and 1T′ phase regions with a spatial step of 0.5 nm. The shaded area indicates an estimate of the 10 nm lateral resolution. The used tip diameter is ~20 nm. The excitation is a 633 nm laser of 1.2 mW. **c** Detected LvF signals when the laser switches on or off, which shows a SNR of 20 dB. **d** Measured LvF amplitudes versus the power of incident light for six experiments with different combinations of $MoTe_2$ crystalline phases (2H or 1T′), film thicknesses (10 nm or 5 nm), and probe tip materials (Au or Si). **e** Temporal stability of the measured LvF signals from $MoTe_2$ samples with different thicknesses. The fluctuations of LvF signals from the 10 nm and 5 nm thick samples do not exceed 8% and 13%, respectively.

the topography was obtained via the f_1 channel (Fig. 2f), which was almost the same as Fig. 2e, meaning that such a weak light excitation did not cause visible expansion or deformation of the sample surface. However, evident LvF signal was probed via the f_2 channel (Fig. 2g) simultaneously. The distribution of the LvF mapping results highly resembled the Gaussian profile of the incident laser spot, showing its optothermal force nature instead of any physical protrusion.

Spatial resolution and compositional resolving capability of LvFM

LvFM possesses unique compositional resolving capability besides its topography resolution identical to general AFM (Fig. 2e, f). This ability is a direct result of LvF associated with and specific to atoms or molecules of varied bonding status, either from different atomic species or from identical atoms of different crystalline phases. The spatial resolution is firstly determined by the probe tip size as that in AFM, and then is further improved by the sensitive tip-sample LvF interaction. A theoretical estimation of the LvF spatial resolution is given in Supporting Information, SI-8, where the LvF contribution of each point ρ on the sample surface to the total tip-sample LvF, i.e., $F'(\rho)/F'$, is numerically calculated. According to the simulation in Fig. S4, an estimate of ~4 nm is determined for the spatial resolution of LvFM, which is even much smaller than the probe tip size (20 nm in diameter). This is unsurprising because the tip-sample vdW force is very sensitive to the tip-sample distance. It also reveals an important fact that, unlike AFM or SNOM whose spatial resolutions are mainly determined by the probe tip size, the LvFM may have a much higher spatial resolution thanks to the tip-sample vdW force interaction.

Then, let us experimentally determine the spatial resolution and compositional resolving capability of LvFM by dealing with, e.g., a $MoTe_2$ film containing two crystalline phases 2H and 1T′. Even though the spatial resolution of LvFM is very high, the two phases of $MoTe_2$ cannot be distinguished without light excitation, since their static vdW force responses are almost the same (Fig. S4). Nevertheless, when an excitation light is applied, the magnitudes of LvF responses of the two phases are both enhanced and exhibit notable difference (Fig. S4), thanks to the distinct bonding forces of molecules in the two phases. This is schematically illustrated in Fig. 3a when the tip scans across the boundary of the two phases. The measured LvF response during this scan is shown in Fig. 3b, from which the practical spatial resolution of LvFM can be estimated to be smaller than 10 nm, which is close to the theoretical estimate above. Note that the spatial resolution of AFM is restrained by deconvolution of tip shape and surface profile, and the spatial resolution of AFM-IR is exaggerated by material thermal diffusion length, while LvFM demonstrates a lateral resolution much smaller than the tip size. Moreover, the sensitivity of LvFM can be manifested by the signal-to-noise ratio (SNR) when the excitation laser is turn on or off. In the above experimental condition (a 633 nm laser excitation of 1.2 mW on the $MoTe_2$ film), the SNR of LvF is as high as 20 dB, as shown in Fig. 3c. We have further tested the dependence of the LvF signal on the tip-sample distance, see Supporting Information, SI-17.

Such a high sensitivity at low excitation power of light is a special advantage of LvFM, which are related to material bonding property, amount of boosted bonds, light intensity, and material absorbance. To investigate these dependencies, we have measured the LvF responses versus incident light power for six samples with different combinations of $MoTe_2$ crystalline phases (2H or 1T′), film thicknesses (10 nm or 5 nm), and probe tip materials (Au or Si), as shown in Fig. 3d. Clearly, when the laser power is above a threshold (~0.6 mW in our experiment), the LvF signals can be detected and increase monotonically

with the increase of the incident power, which are in good agreement with the theoretical prediction in Fig. 1d. In addition, under the same light power and with the same film thickness, the 2H phase has stronger LvF response than 1T′ phase, because the absorption coefficient of the metallic 1T′ phase is larger so that the light transmitting through it from the bottom and arriving at the top surface is weaker. Hence, the light-enhanced thermal motions of the 1T′ phase molecules are weaker. For the same phase of $MoTe_2$, thicker film produces stronger LvF, because more light energy is absorbed to boost more bonds. Furthermore, when an Au-coated probe is used instead of the Si probe, larger LvF signal can be collected, which can be explained by the fact that the Hamaker constant of Au is larger than that of Si so that the tip-sample LvF interaction is stronger. All these observations validate the LvFM principle and demonstrate its sensitivity and performance.

Moreover, we have tested the temporal stability of the LvFM system. As shown in Fig. 3e, during the measurements in 15 s, the fluctuations of the LvF signals from the 10 nm thick and 5 nm thick $MoTe_2$ films do not exceed 8% and 13%, respectively, which are satisfactory for practical application. It also implies that thicker samples are preferable to get better stability.

Application of LvFM for compositional discrimination of materials

LvFM meets urgent needs of composition and nanodefects characterization of materials, particularly 2D materials[30,31], such as the occasion of inserting a nanoscale metal-phase buffer layer between the channel and electrode in manufacturing field effect tubes[32]. Many nanodefects including nanobubbles, stacks, vacancies, grain boundaries, impurities, and adsorptions are associated with material preparation and device fabrication[33]. They are not completely characterizable with currently available technologies. For example, X-ray diffraction (XRD) is good at determination of crystalline structures but lack of spatial resolution. Electron microscopy possesses the highest morphological resolution better than 1 nm, but destructive sample preparation is needed for composition discrimination[34]. AFM-IR is suffering from relatively low resolution and strict requirement of wavelength provision[35]. In contrast, boosting material bonding force by light to generate LvF in LvFM requires relatively weak light excitation that are possibly provided by lasers of almost any wavelength. Light absorption mechanisms ranging from inter-band transitions, impurity absorption, molecular vibrations and rotations all work for LvFM.

In the following, we conduct a series of experiments to demonstrate the use of LvFM to discriminate the compositions of samples composed of various materials. The first experiment is to distinguish the 2H and 1T′ crystalline phases in a 10 nm thick $MoTe_2$ film, the same sample as that characterized in Fig. 3, under the excitation of a 633 nm laser of 1.2 mW. The topography and LvF distribution simultaneously obtained by 300 × 300 pixels in an area of 20 μm × 20 μm within 14 min are given in Fig. 4a, b, respectively. The topography shows that the sample is an atomically flat film with surface fluctuation smaller than 0.2 nm, but its two phases cannot be distinguished. In contrast, the LvF mapping results clearly discriminate the different regions of 2H and 1T′ phases. The characterization results are further confirmed by Raman peaks at 235 cm^{-1}, attributed to in-plane E_{2g} mode of 2H phase, and 124 cm^{-1} (A_g) and 163 cm^{-1} (B_g) peaks associated with 1T′ phase (Fig. 4c), as well as by its confocal Raman mapping (Fig. 4d). XRD characterizations (Supporting Information, SI-9) have also been conducted to cross check the results.

Furthermore, since LvFM is a broadband technique insensitive to the wavelength of excitation light, we have performed LvF mapping by tuning the excitation laser wavelength in the range of 500–900 nm (Supporting Information, SI-10). The LvF mapping results and the deduced LvF contrast U_H/U_T are given in Fig. S6 and Fig. 4f, respectively, which show good LvF contrast in a broad band. In addition, we have measured the absorbance of 2H and 1T′ phases, as shown in Fig. 4e. Their difference (the green dashed line in Fig. 4e) agrees well in trend with the experimentally obtained LvF contrast (Fig. 4f) in the same spectral range, validating the optothermal enhancement origin of LvFM.

Then we use LvFM to characterize a heteromaterial sample composed of two types of 2D materials, h-BN and multilayer WS_2 nanosheets. By raster scan, the topography of the sample is obtained (Fig. 4g), from which some coarse structures can be observed but the composing materials are unknown. Similarly, the absorbance of h-BN and WS_2 can be measured (Fig. 4h), whose difference determines their LvF contrast. The LvF mapping image under an excitation wavelength of 633 nm is given in Fig. 4i, and more mapping results under excitation wavelengths of 600 nm and 680 nm are given in Supporting Information, SI-11. In all these images, the h-BN and WS_2 regions can be clearly distinguished with a high spatial resolution of ~10 nm.

Moreover, we have characterized additional five samples composed of various materials including organics, metals, metal oxides, inorganic compounds, etc. to show the wide material applicability and performance of LvFM. The experimental details and results can be found in Supporting Information, SI-12-SI-16.

Discussion

Most versions of AFM developed so far work by manipulating tip-sample interactions or cantilever oscillations, apparently lack of contributions from intrinsic material property reflected by bonding force, an even more important type of atomic force. We propose here the concept of LvF, which manipulates bonding forces by light boosting local thermal motions of molecules beneath an AFM tip. As a result, a light-modulated tip-sample vdW force is generated and enhanced, and the enhancement factor is sensitively dependent on the atomic species composing the specimen, allowing for compositional discrimination. This makes LvFM particularly attractive for at least three facts: (i) high compositional resolving capability represented by, for example, a 20 dB SNR on a $MoTe_2$ film under the excitation of a 633 nm laser of 1.2 mW; (ii) high lateral spatial resolution down to sub-10 nm, which is even smaller than the tip size of 20 nm; (iii) low excitation laser power requirement and the wide applicability in a broad spectral range and for various types of materials. These unique features exhibit that LvFM may be widely used for characterizing materials, particularly 2D materials, which are promising candidates for electronic and optoelectronic chip materials.

Methods

Specifications of the LvFM system

A tunable laser (Topaz-fps-50, BWT) incorporated with an acousto-optic tunable filter (AOTF) is employed as the light source. The output pulse width is 100 ps, which is modulated by a square wave at a chopping frequency f_m by an acousto-optic modulator (AOM, AOMO 3080-125, Gooch & Housego). An aperture is mounted to select the zeroth order beam of the AOM, as its propagation direction is independent of the wavelength. A linear polarizer (LP) and a half-wave plate (λ/2 WP) are used to adjust the polarization state of the laser beam. After passing through a beam splitter (BS), the laser beam is focused onto the sample surface from the bottom through an objective (Nikon, CF Plan 100x, NA = 0.95). A precision stage (P-517.3CL, Physik Instrumente) holding the sample moves laterally with a minimum step of 0.3 nm to realize the *x*-*y* scan. The mechanical vibration of a probe (PPP-NCHAu, Nanosensor or NSG10, TipsNano) is monitored by an AFM (NTEGRA, NT-MDT) with an optical lever. A sideband demodulation technique is applied to extract the LvF signal, where two lock-in amplifiers (HF2LI, Zurich Instruments) are used to probe the first and second-order eigenmode vibration signals of the cantilever. A LED and a CCD are used for sample illumination and microscopic imaging, respectively, both of which are integrated inside an inverted microscope (Olympus, IX81).

https://doi.org/10.1038/s41467-024-53461-5

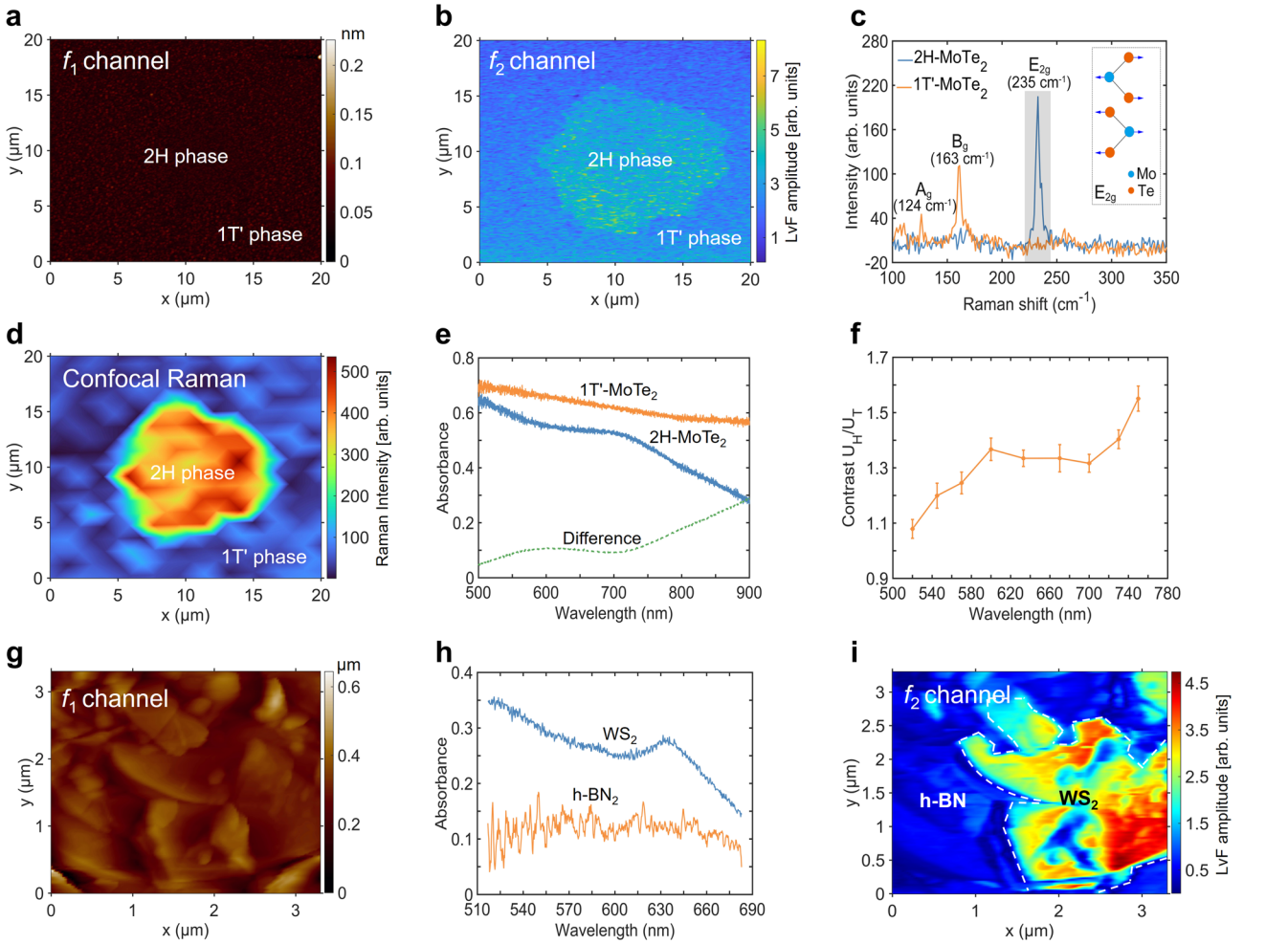

Fig. 4 | Discrimination of heterophases and heterogeneous compositions of materials with LvFM. a Topography of a 10 nm thick $MoTe_2$ film with two crystalline phases measured with LvFM f_1 channel, indicating the surface flatness. **b** LvF mapping results obtained from f_2 channel, where the 2H phase and 1T′ phase regions are clearly discriminated. **c** Raman spectra measured from different phases, where the fingerprint Raman peaks distinguish the 2H and 1T′ phases. **d** Confocal Raman mapping images obtained with Raman shifts from 225 cm^{-1} to 245 cm^{-1}, as indicated by the shaded area in (**c**). **e** Measured absorbance spectra of the 2H phase (blue curve) and 1T′ phase (orange curve) of the $MoTe_2$ film, whose difference indicated by the green dashed line is the origin of the LvF signal contrast. **f** LvF contrast U_H/U_T of the two phases at different excitation wavelengths, where U_H and U_T refer to the averaged LvF signal strengths in the 2H and 1T′ regions, respectively. The contrast curve's trend is in good agreement with the green curve in (**e**), showing the possible selection of excitation light in a wide band. **g** Topography of a heteromaterial composed of multilayer h-BN and WS_2 nanosheets, which is measured via LvFM f_1 channel. **h** Measured absorbance spectra of the multilayer h-BN and WS_2. **i.** LvF mapping results obtained from f_2 channel under the excitation wavelength of 633 nm, where the h-BN and WS_2 areas are clearly seen with their boundary indicated by white dash lines.

Preparation of the $MoTe_2$ sample

A sample of multi-layer $MoTe_2$ nanoflakes featuring in-plane 2H-1T′ $MoTe_2$ homojunctions was fabricated utilizing Mo nanofilm as precursor via chemical vapor deposition (CVD). To initiate the process, Mo nanofilms were deposited onto a fused silica substrate by e-beam evaporation. The substrate, positioned face-down, was then carefully situated within the heating zone at the core of an alumina boat containing Te slugs (99.999%, Sigma Aldrich). Carrier gases comprising argon (99.999%) and hydrogen (99.999%) were employed during the reaction, with both gases flowing at a constant rate of 20 sccm (standard cubic centimeters per minute). The furnace was gradually heated to 600 °C over a period of 15 min (with a linear ramp rate of approximately 38.3 °C per min) and maintained at this temperature for 30 min to enable synthesis of the desired in-plane 2H-1T′ $MoTe_2$ homojunctions. Subsequently, 10 min after the reaction, the furnace lid was opened to expedite the cooling process, allowing it to reach room temperature rapidly. X-ray diffraction (XRD, smartlab, Rigaku) characterization was performed, as shown in Supporting Information, SI-9, confirming the existence of 1T′ phase and 2H phase $MoTe_2$.

Data availability

The data supporting the findings of this study have been interpreted, verified, and presented in the main text and Supplementary Information. All other information can be obtained from the corresponding author upon request.

Code availability

The data analysis supporting the findings of this study are interpreted, verified, and presented in the main text and Supplementary Information. All other information can be obtained from the corresponding author upon request.

References

1. Binnig, G., Quate, C. F. & Gerber, C. Atomic force microscope. *Phys. Rev. Lett.* **56**, 930–933 (1986).

2. Zou, X. et al. Imaging based on metalenses. *PhotoniX* **1**, 2 (2020).
3. Gross, L. et al. Bond-order discrimination by atomic force microscopy. *Science* **337**, 1326–1329 (2012).
4. Zhang, J. et al. Real-Space Identification of Intermolecular Bonding with Atomic Force Microscopy. *Science* **342**, 611–614 (2013).
5. Parsegian, V. A. *Van der Waals Forces: A Handbook for Biologists, Chemists, Engineers, and Physicists* (Cambridge University Press, 2005).
6. Hinterdorfer, P. & Dufrêne, Y. F. Detection and localization of single molecular recognition events using atomic force microscopy. *Nat. methods* **3**, 347–355 (2006).
7. Custance, O., Perez, R. & Morita, S. Atomic force microscopy as a tool for atom manipulation. *Nat. Nanotechnol.* **4**, 803–810 (2009).
8. Zhao, L.-Y. et al. Ultrafast modulation of valley dynamics in multiple WS_2 – Ag gratings strong coupling system. *PhotoniX* **3**, 5 (2022).
9. Gou, J. et al. Two-dimensional ferroelectricity in a single-element bismuth monolayer. *Nature* **617**, 67–72 (2023).
10. Friedbacher, G., Hansma, P. K., Ramli, E. & Stucky, G. D. Imaging powders with the atomic force microscope: from biominerals to commercial materials. *Science* **253**, 1261–1263 (1991).
11. Drake, B. et al. Imaging crystals, polymers, and processes in water with the atomic force microscope. *Science* **243**, 1586–1589 (1989).
12. Mathurin, J. et al. Photothermal AFM-IR spectroscopy and imaging: Status, challenges, and trends. *J. Appl. Phys.* **131** (2022).
13. Cui, T. et al. Spin-symmetry-selective generation of ultracompact optical vortices in nanoapertures without chirality. *Small Struct.* **1**, 2000008 (2020).
14. Sun, L. et al. Probing the photonic spin–orbit interactions in the near field of nanostructures. *Adv. Funct. Mater.* **29**, 1902286 (2019).
15. Rodríguez, T. R. & García, R. Compositional mapping of surfaces in atomic force microscopy by excitation of the second normal mode of the microcantilever. *Appl. Phys. Lett.* **84**, 449–451 (2004).
16. Kawai, S. et al. Systematic achievement of improved atomic-scale contrast via bimodal dynamic force microscopy. *Phys. Rev. Lett.* **103**, 220801 (2009).
17. Dupont, M. F., Elbourne, A., Mayes, E. & Latham, K. Measuring the mechanical properties of flexible crystals using bi-modal atomic force microscopy. *Phys. Chem. Chem. Phys.* **21**, 20219–20224 (2019).
18. Huang, L. et al. Nanoscale chemical and mechanical heterogeneity of human dentin characterized by AFM-IR and bimodal AFM. *J. Adv. Res.* **22**, 163–171 (2020).
19. Sun, Y., Hu, Z., Zhao, D. & Zeng, K. Mechanical properties of microcrystalline metal–organic frameworks (MOFs) measured by bimodal amplitude modulated-frequency modulated atomic force microscopy. *ACS Appl. Mater. interfaces* **9**, 32202–32210 (2017).
20. Amo, C. A., Perrino, A. P., Payam, A. F. & Garcia, R. Mapping elastic properties of heterogeneous materials in liquid with angstrom-scale resolution. *ACS Nano* **11**, 8650–8659 (2017).
21. Martínez-Martín, D., Herruzo, E. T., Dietz, C., Gomez-Herrero, J. & Garcia, R. Noninvasive protein structural flexibility mapping by bimodal dynamic force microscopy. *Phys. Rev. Lett.* **106**, 198101 (2011).
22. Giessibl, F. J. Forces and frequency shifts in atomic-resolution dynamic-force microscopy. *Phys. Rev. B* **56**, 16010 (1997).
23. Lantz, M. et al. Quantitative measurement of short-range chemical bonding forces. *Science* **291**, 2580–2583 (2001).
24. Liu, S.-F. et al. 3D nanoprinting of semiconductor quantum dots by photoexcitation-induced chemical bonding. *Science* **377**, 1112–1116 (2022).
25. Li, B. et al. Probing van der Waals interactions at two-dimensional heterointerfaces. *Nat. Nanotechnol.* **14**, 567–572 (2019).
26. Moy, V. T., Florin, E.-L. & Gaub, H. E. Intermolecular forces and energies between ligands and receptors. *Science* **266**, 257–259 (1994).
27. Israelachvili Jacob, N. *Intermolecular and Surface Forces: Revised* 3rd ed. (Academic Press, 2011).
28. Garcıa, R. & Perez, R. Dynamic atomic force microscopy methods. *Surf. Sci. Rep.* **47**, 197–301 (2002).
29. Landau, D. & Binder, K. *A Guide to Monte Carlo Simulations in Statistical Physics* (Cambridge University Press, 2021).
30. Sun, Y.-K. et al. Non-Abelian Thouless pumping in photonic waveguides. *Nat. Phys.* **18**, 1080–1085 (2022).
31. Zhang, X.-L. et al. Non-Abelian braiding on photonic chips. *Nat. Photonics* **16**, 390–395 (2022).
32. Cho, S. et al. Phase patterning for ohmic homojunction contact in $MoTe_2$. *Science* **349**, 625–628 (2015).
33. Wu, Z. T. & Ni, Z. H. Spectroscopic investigation of defects in two-dimensional materials. *Nanophotonics* **6**, 1219–1237 (2017).
34. Das, S., Chen, H. Y., Penumatcha, A. V. & Appenzeller, J. High performance multilayer MoS_2 transistors with scandium contacts. *Nano Lett.* **13**, 100–105 (2013).
35. Dazzi, A. & Prater, C. B. AFM-IR: technology and applications in nanoscale infrared spectroscopy and chemical imaging. *Chem. Rev.* **117**, 5146–5173 (2017).

Acknowledgements

This work is supported by the National Natural Science Foundation of China under grant numbers 62175121 (B.B.) and 61960206003 (H.-B.S.), and by Tsinghua-Foshan Innovation Special Fund under grant number 2021THFS0102 (H.-B.S.).

Author contributions

Y.-X.H., B.B., and H.-B.S. conceived the idea, proposed the theoretical framework, designed the experiments, analyzed the data, and wrote the manuscript. Y.-X.H. conducted most of the experimental research, including the LvFM setup establishment, sample preparation, and experimental characterization. J.-Y.Z., J.T.H., and P.-Y.F. participated in sample preparation, experimental characterization, and LvFM system construction. All authors discussed the results together and contributed to the preparation of the manuscript. B.B. and H.-B.S. led the project.

Competing interests

The authors declare no competing interests.

Additional information

Supplementary information The online version contains supplementary material available at https://doi.org/10.1038/s41467-024-53461-5.

Correspondence and requests for materials should be addressed to Benfeng Bai or Hong-Bo Sun.

Peer review information *Nature Communications* thanks Yun-Sheng Chen, Jieun Yang and the other, anonymous, reviewer(s) for their contribution to the peer review of this work. A peer review file is available.

Reprints and permissions information is available at http://www.nature.com/reprints

Publisher's note Springer Nature remains neutral with regard to jurisdictional claims in published maps and institutional affiliations.

Open Access This article is licensed under a Creative Commons Attribution-NonCommercial-NoDerivatives 4.0 International License, which permits any non-commercial use, sharing, distribution and reproduction in any medium or format, as long as you give appropriate credit to the original author(s) and the source, provide a link to the Creative Commons licence, and indicate if you modified the licensed material. You do not have permission under this licence to share adapted material derived from this article or parts of it. The images or other third party material in this article are included in the article's Creative Commons licence, unless indicated otherwise in a credit line to the material. If material is not included in the article's Creative Commons licence and your intended use is not permitted by statutory regulation or exceeds the permitted use, you will need to obtain permission directly from the copyright holder. To view a copy of this licence, visit http://creativecommons.org/licenses/by-nc-nd/4.0/.

© The Author(s) 2024